

Impact of nitrogen on the charge-to-spin conversion efficiency in antiferromagnetic Mn₃PtN compared to Mn₃Pt thin films

Nitipriya Tripathi ^{*,†} and Shrawan K. Mishra 

School of Materials Science and Technology, Indian Institute of Technology (BHU), Varanasi-221005, India

Yoshio Miura  and Shinji Isogami ^{*,‡}

Center for Magnetic and Spintronic Materials, National Institute for Materials Science (NIMS), Tsukuba 305-0047, Japan



(Received 17 January 2024; revised 6 April 2024; accepted 13 May 2024; published 4 June 2024)

The bilayer structures consisting of Mn₃PtN (5 nm)/CoFeB(3 nm) and Mn₃Pt(5 nm)/CoFeB(3 nm) were fabricated via magnetron sputtering to investigate the role of nitrogen on charge-to-spin conversion efficiency in the noncollinear antiferromagnets (AFMs). The crystal structure of Mn₃PtN (MPN) without N is consistent with that of Mn₃Pt (MP) with $L1_2$ -ordered structure, which allows us to study the different charge-to-spin conversion efficiency for AFMs with and without N. The spin-torque ferromagnetic resonance and second-harmonic Hall measurements were performed for both samples. It was revealed that the spin Hall angle (θ_{SH}) of the MPN with spin polarization in the y direction was observed to be ~ 0.033 , exceeding the corresponding value of MP (~ 0.025), which was qualitatively supported by the first-principles calculation. These results led us to conclude that N plays a crucial role in stabilizing the noncollinear antiferromagnetic structure and creating an electronic state advantage for the enhanced θ_{SH} .

DOI: [10.1103/PhysRevB.109.224406](https://doi.org/10.1103/PhysRevB.109.224406)

I. INTRODUCTION

The manipulation of magnetization in ferromagnets (FMs) by spin current has been a key technology in recent spintronics. There are some origins for the charge-to-spin conversion phenomena, which are the bulk spin Hall effect (SHE) [1] that is typically observed in the nonmagnetic heavy metals and the Rashba-Edelstein effect (REE) [2] originating from inversion symmetry breaking at the interfaces of bilayer structures. The spin current by these phenomena provides the magnetization of adjacent FMs with spin-orbit torques (SOTs), leading to the efficient current-induced magnetization switching in spintronic devices such as nonvolatile memories with significantly low power consumption.

In recent years, noncollinear antiferromagnets (AFMs) have received more attention as one of the new spin sources whose mechanisms are different from the conventional SHE and REE. The specific characteristic of charge-to-spin conversion in the AFMs is the appearance of not only y -polarized spin (σ_y) but also x - and z -polarized spins (σ_x and σ_z), originating from the low-symmetry triangular magnetic structures, the magnetic moment of which has both in-plane and out-of-plane components with respect to the current flow [3–6]. These findings bring so-called anisotropic SOTs, leading to the field-free magnetization switching of perpendicular magnetization [5], which strongly contributes to the high integration of nonvolatile memories. In addition, the recent study also suggests

the other origins of field-free magnetization switching such as interfacial Dzyaloshinskii-Moriya interaction and cubic magnetic anisotropy [7]. In order to realize the highly integrated devices based on such advantages in AFMs, the next topic to focus on is boosting the charge-to-spin conversion efficiency by material engineering such as elemental doping, ordering, and alloying in AFMs.

Although the charge-to-spin conversion in the $L1_2$ -ordered Mn₃Pt compound with a Néel temperature of 475 K has been extensively studied [3–5] as one of the metallic AFMs like Mn₃Ir [8,9], transition-metal nitrides (TMNs) with antiperovskite structure denoted by A_3BN (in which N occupies the body-centered site of the face-centered-cubic structure formed by the sublattices of transition metals A and B) have been attracting more attention due to their various magnetic and spintronic properties [10–15]: inverse (negative) magnetoresistance [16–20], current-induced spin-transfer torque–spin-orbit switching [21–25], thermoelectric conversion [26–28], propagation of magnetic domains and skyrmions [29–33], and giant magnetostriction [34]. These properties in the TMNs are generally attributed to the topological features of electronic band structures [35], resulting from the hybridization effects between the A and N ions as well as B and N ions. In particular, for $A = \text{Mn}$, Mn_3BN ($B = \text{Pt}$, Ir , Cu , Ni , etc.), the noncollinear AFM structure and the efficient anomalous Hall effect (AHE) as well as anomalous Nernst effect (ANE) are predicted by first-principles calculations within the framework of AFM spintronics [36,37]. It should be highlighted that the field-free current-induced magnetization switching of ferromagnetic layers triggered by SOTs has been demonstrated in the bilayer systems with noncollinear AFMs such as Mn₃GaN [38] and Mn₃SnN [39]. However, the

*These authors contributed equally to this work.

†Corresponding author: nitipriyatripathi.rs.mst20@itbhu.ac.in

‡Corresponding author: isogami.shinji@nims.go.jp

role of N for enhancing the SOTs in the TMNs has not been fully investigated to date.

In this study, the charge-to-spin conversion in the $\text{Mn}_3\text{PtN}/\text{CoFeB}$ bilayer systems was investigated by spin-torque ferromagnetic resonance (ST-FMR) and second-harmonic Hall measurements in comparison to the control $\text{Mn}_3\text{Pt}/\text{CoFeB}$ systems. Note that the host crystal structure of Mn_3PtN without N atoms and its noncollinear AFM structure are consistent with Mn_3Pt [40]. Therefore, it is possible to extract the impact of N on charge-to-spin conversion by comparing these bilayer systems, in which the only difference is the presence of N. As a result, it was revealed that the σ_y dominates the polarized spins converted from the charge current in both systems, while the components of σ_x and σ_z slightly coexist in the Mn_3PtN system. The Mn_3PtN system showed an $\sim 32\%$ increase in the spin-Hall angle (θ_{SH}) compared to the Mn_3Pt system, which is the impact of N ordering at the preferential site of Mn_3PtN with antiperovskite structure. The first-principles calculation of the spin Hall conductivity qualitatively supported the experimental results.

II. METHODS

A. Experimental procedure

The multilayer structure, $\text{MgO}(001)\text{sub.}/\text{Mn}_3\text{PtN}$ (hereinafter referred to as MPN) (5, 7, and 10)/ CoFeB (hereinafter referred to as CFB) (3)/ MgO (3) (thickness unit in nanometers), were deposited using the dc and rf magnetron sputtering systems with the base pressure of less than 1×10^{-6} Pa. For the deposition of MPN, the reactive nitride sputtering technique was employed, and the N_2 gas-flow ratio that is defined by $N_2/(\text{Ar} + N_2)$ was 10%. The growth temperature of MPN was optimized to be 723 K. The CFB and MgO layers were deposited at room temperature. The atomic ratios of MPN and CFB were evaluated to be (Mn : Pt = 3 : 1) and (Co : Fe : B = 1 : 3 : 1), respectively, by x-ray fluorescence. For a comparison, the same multilayer structure was fabricated by replacing the MPN layer with Mn_3Pt (hereinafter referred to as MP) layer. The structural analysis was performed by x-ray diffraction (XRD) with the $\text{Cu-K}\alpha$ radiation. The crystal-order parameter (S) was estimated using the formula $S = \sqrt{\frac{I_{001}^{\text{Obs.}}/I_{002}^{\text{Obs.}}}{I_{001}^{\text{Cal.}}/I_{002}^{\text{Cal.}}}}$, where $I_{001(002)}^{\text{Cal.}(Obs.)}$ represents the integral intensity of the XRD from the 001(002) plane given by the calculation (experimental profile). The detailed procedure has been shown in previous papers [41,42]. The surface roughness (R_a) and the magnetic property of the CFB layer were evaluated using the atomic force microscope and the vibrating sample magnetometer (VSM), respectively. Microfabrication was performed using Ar ion milling and photolithography to fabricate the wire devices for ST-FMR and second-harmonic Hall measurements, the size of which was 6- μm width and 20- μm length. These measurements were performed at room temperature.

B. Computational details

The first-principles calculations of MP and MPN were performed by the QUANTUM ESPRESSO code [43]. The projector augmented-wave pseudopotentials [44] were used for the atomic potentials of Mn, Pt, and N with the plane-wave and

the charge-density cutoff energies 60 and 400 Ry, respectively. We adopted the generalized gradient approximation [45] for the exchange and correlation energy including the spin-orbit interaction with $16 \times 16 \times 16$ k points in the first Brillouin zone. The lattice parameters of both MP and MPN were taken from the experimental value for the 5-nm-thick MPN film, which were slightly distorted to the tetragonal unit cell $a = 0.40046$ nm and $c/a = 0.9862$. We performed the calculations of spin-Hall conductivity (σ) for the MP and MPN with Γ_{4g} -type noncollinear AFM structure based on the linear response theory [46,47] using the following equation:

$$\sigma_{\alpha\beta}^{\gamma}(E) = \frac{e}{V} \sum_{\mathbf{k}} \Omega_{\alpha\beta}^{\gamma}(\mathbf{k}, E). \quad (1)$$

$\Omega_{\alpha\beta}^{\gamma}(\mathbf{k}, E)$ is the spin Berry curvature given by [48]

$$\Omega_{\alpha\beta}^{\gamma}(\mathbf{k}, E) = 2 \frac{\hbar^2}{m_e^2} \sum_{n>m} [f_{kn}(E) - f_{km}(E)] \times \frac{\text{Im}(\langle \mathbf{k}m | (\hat{p}_{\beta} \hat{s}_{\gamma} + \hat{s}_{\gamma} \hat{p}_{\beta}) | \mathbf{k}n \rangle \langle \mathbf{k}n | \hat{p}_{\alpha} | \mathbf{k}m \rangle)}{(\varepsilon_{kn} - \varepsilon_{km})^2}, \quad (2)$$

where V is the volume of the unit cell, m_e is the electron mass, m and n are the occupied and unoccupied band indices, \hat{p}_{α} (\hat{p}_{β}) is the α (β)-axis component of the momentum operator, \hat{s}_{γ} is the spin angular momentum operator with the spin quantum axis along the γ direction, $|\mathbf{k}n\rangle$ is the eigenstate with the eigenenergy ε_{kn} , and $f_{kn}(E)$ is the occupation function for the band n and wave vector \mathbf{k} at the energy (E) relative to the Fermi level (E_F). In the spin Hall conductivity calculations, the tight-binding Hamiltonian was constructed by the maximally localized Wannier function basis with the WANNIER90 code [49,50]. Then, the σ was computed using $100 \times 100 \times 100$ points in the first Brillouin zone.

III. RESULTS AND DISCUSSION

A. Characterization of Mn_3PtN and Mn_3Pt thin films

Figure 1(a) illustrates the unit cell of MPN, displaying the magnetic structure of Mn. A possible Γ_{4g} -type noncollinear AFM structure, commonly known as head-to-head and tail-to-tail configuration on the (111) plane, could be formed in the present film. Figure 1(b) shows the out-of-plane XRD profile for the $\text{MgOsub.}/\text{MPN}(5)/\text{CFB}(3)/\text{MgO}(3)$. The diffraction peaks observed at $2\theta/\omega \approx 23^\circ$ and 46° originate from the (001) superlattice and (002) fundamental lattice, respectively. The result of fitting with pseudo-Voigt function is shown by the dashed line, and the S of Pt, Mn, and N in the 5-nm-thick MPN layer was estimated to be $S \approx 0.77$, indicating a relatively high level of atomic order. An element-selective synchrotron anomalous XRD was additionally performed to focus on the atomic order of Mn in the MPN [51]. These results show that the unit cell depicted in Fig. 1(a) could be a dominant crystal structure in the present MPN film. Note that the XRD from the 3-nm-thick CFB was not detected, corresponding to an amorphous and/or nanocrystalline structure. The inset of Fig. 1(b) displays the surface morphology for the 25-nm-thick MPN single layer, the R_a value of which

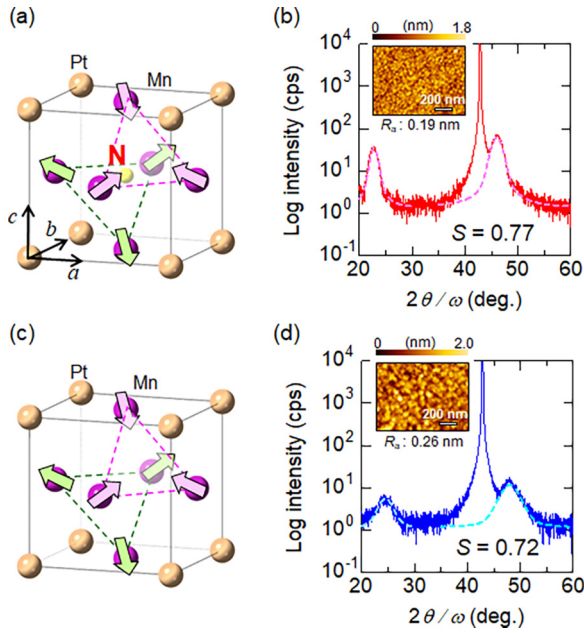


FIG. 1. (a) Unit cell of Mn_3PtN (MPN) crystal with antiperovskite structure together with the possible Γ_{4g} -type magnetic structure. (b) Out-of-plane XRD profile for the stacking of MgO-sub./MPN(5)/CoFeB(3)/MgO(2) (in nm). The dashed lines represent the fitting curves with pseudo-Voigt function to estimate the degree of order (S). Inset shows an atomic force microscopy image of the 25-nm-thick MPN surface. (c), (d) The same as 1(a) and 1(b), but regarding the Mn_3Pt (MP).

was remarkably small, indicating a smooth interface could be expected between the present MPN(5)/CFB(3) sample.

Figure 1(c) displays the unit cell of MP with an $L1_2$ -ordered structure. The possible magnetic structure of Mn shown by the arrow is consistent with that of MPN, namely, a noncollinear AFM configuration of the Γ_{4g} type. Figure 1(d) shows the out-of-plane XRD profile of the MgO-sub./MP(5)/CFB(3)/MgO(3). Similar to the bilayer system with MPN [Fig. 1(b)], the observed XRD peaks originated from the (001) superlattice and (002) fundamental lattice. The $S \approx 0.72$ was obtained, indicating that the dominant phase in the present MP layer is $L1_2$. The R_a of 30-nm-thick MP single layer was comparable to that of MPN. Note that the out-of-plane lattice constant of the 5-nm-thick MPN ($c \approx 0.395$ nm) was larger than that of the MP ($c \approx 0.379$ nm), which was consistent with the findings of a previous report [39]. The in-plane lattice constant (a) of the 5-nm-thick MPN was estimated to be $a \approx 0.400$ nm; therefore, the present 5-nm-thick MPN film involved tetragonal distortion along the out-of-plane direction with $c/a \approx 0.99$. This tetragonal distortion might originate from the in-plane tensile strain at the interface between the MgO substrate (with $a \approx 0.420$ nm) [51].

B. Possible magnetic structures of Mn_3PtN and Mn_3Pt thin films

In order to assess the possible magnetic structure of MPN and MP, magnetic properties and AHE were investigated. The out-of-plane magnetic hysteresis loop of the 5-nm-thick

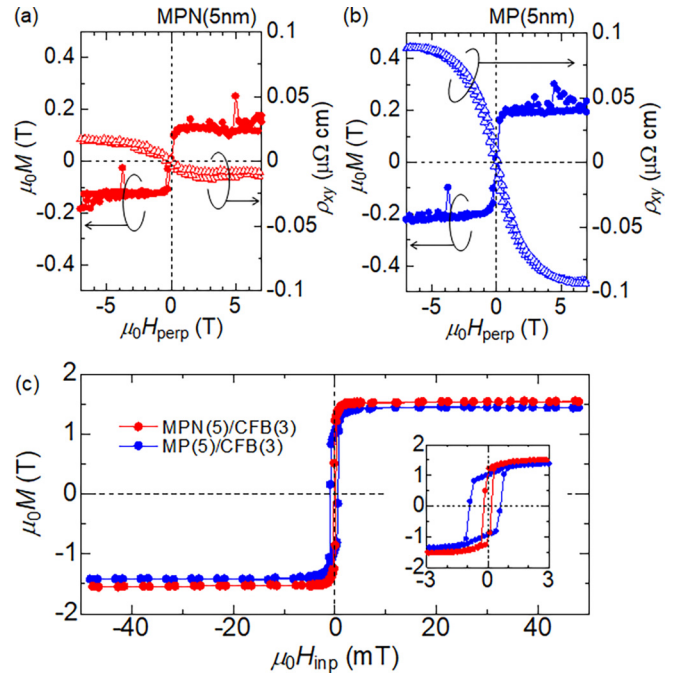


FIG. 2. (a), (b) Magnetic hysteresis (solid circles) and anomalous Hall resistivity (ρ_{xy}) (open triangles) for the 5-nm-thick MPN (a) and the 5-nm-thick MP single layers (b) as a function of the out-of-plane magnetic field (H_{perp}) at room temperature. (c) Magnetic hysteresis for the stacking of MgOsub./MPN(5)/CFB(3)/MgO(2) (red) and that of MgO sub./MP(5)/CFB(3)/MgO(2) (blue) (in nm) as a function of in-plane magnetic field (H_{inp}) at room temperature. The inset represents the enlarged magnetic hysteresis loops near the zero field.

MPN single layer is shown by the solid symbols in Fig. 2(a), where the diamagnetic background of the MgO substrate was subtracted. Soft magnetic switching was observed around the zero field, consistent with the previous reports for the Mn_3Pt films with a thickness of 12–15 nm [3,5]. The present film involves tetragonal distortion, with the lattice constant ratio of $c/a \approx 0.99$ as mentioned above. Thus, it is inferred that the soft magnetic behavior observed around the zero field in Fig. 2(a) is due to the uncompensated magnetic moment of Mn originating from the distortion. The anomalous Hall resistivity (ρ_{xy}) is plotted as a function of the magnetic field pointing in the out-of-plane direction and indicated by open symbols in Fig. 2(a). Based on the theoretical prediction [52,53], the finite AHE implies the potential existence of a noncollinear AFM structure of the Γ_{4g} type, as shown in Fig. 1(a).

Figure 2(b) presents the same experiments depicted in Fig. 2(a), but regarding the 5-nm-thick MP single layer. Comparable to the MPN scenario, a significant uncompensated Mn moment might contribute to the soft magnetic behavior observed at near-zero field. The saturation magnetization of the MP film was $\mu_0 M_s \approx 0.2$ T, which was almost 10 times magnitude larger than that of the 15-nm-thick MP film on the MgO substrate in another report [3,5]. The interpretation for this discrepancy has not been fully understood; however, based on the thickness-dependent c/a values, it is speculated that the component of uncompensated Mn moment could be more prominent in the thinner MP film compared to the thicker film. For further details, refer to Ref. [51]. Based

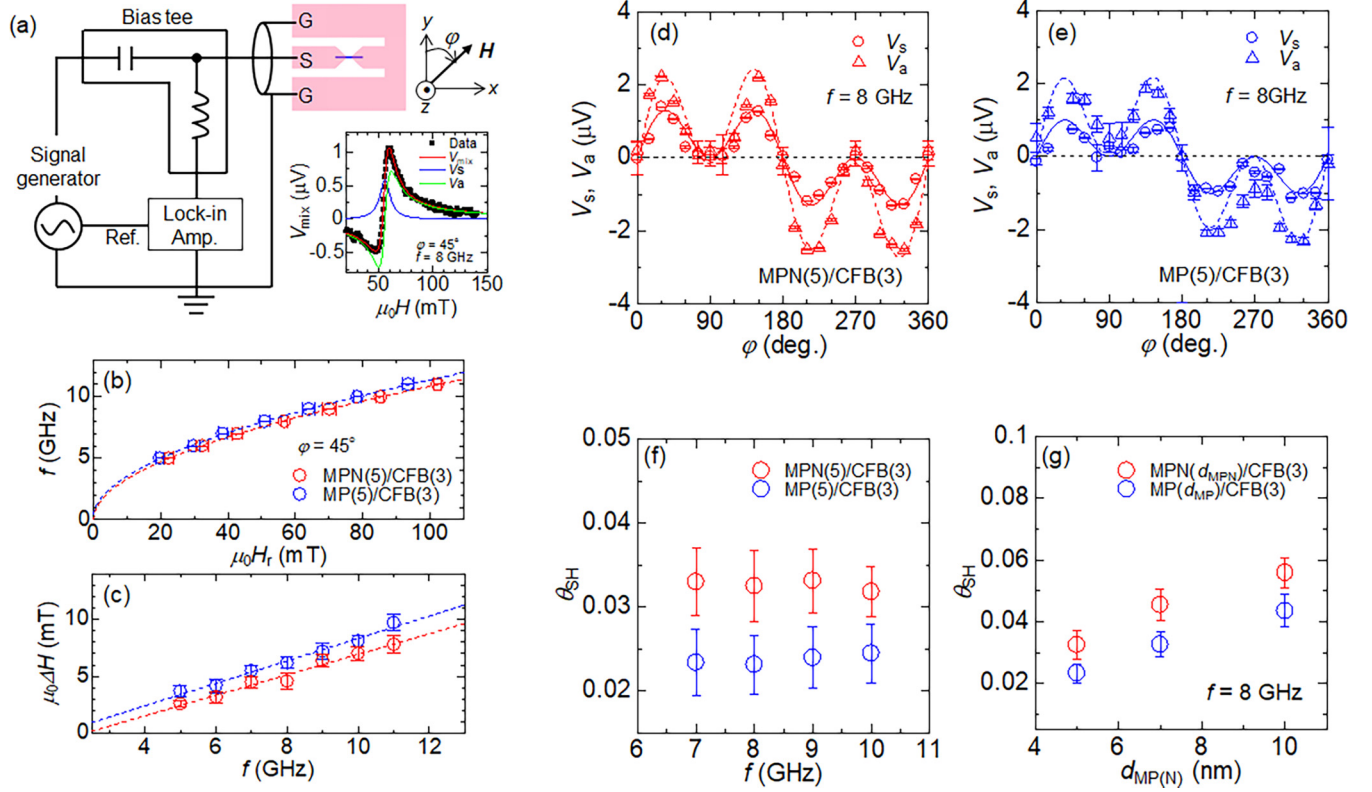


FIG. 3. (a) Spin-torque ferromagnetic resonance (ST-FMR) setups together with the typical field-domain spectrum (V_{mix}) recorded at the in-plane magnetic field (H) with the azimuthal angle of $\varphi = 45^\circ$. The blue and green solid lines represent the Lorentzian and anti-Lorentzian fitting results using Eq. (3), respectively. (b), (c) Relationship between the resonance field (H_r) and the applied rf frequency (f) (b), and the f and ST-FMR linewidth (ΔH) (c) for both MgOsub./MPN(5)/CFB(3)/MgO(2) and MgOsub./MP(5)/CFB(3)/MgO(2) (in nanometers). (d), (e) φ dependence of symmetric Lorentzian (V_s) and antisymmetric Lorentzian (V_a) components for the same samples. The solid and dashed lines represent the fitting curve using Eqs. (6) and (7), respectively. (f), (g) Dependences of spin Hall angles (θ_{SH}) on f (f) and the thickness of MPN and MP layers (g) estimated using Eq. (8), which is dominated by the spin torque originating from the polarization in y direction.

on these magnetic properties and AHE results, it should be highlighted that the Γ_{4g} -type noncollinear AFM structure is predominant in both MPN and MP.

Figure 2(c) shows the magnetic hysteresis loops at room temperature for the samples MPN/CFB and MP/CFB bilayers. The $\mu_0 M_s$ and coercivity of the CFB layer differed between the MPN/CFB and MP/CFB, while the lateral shift resulting from the interlayer exchange interaction was tiny for both samples. Therefore, it is expected that there is not a large difference in the spin injection efficiency at their interfaces at room temperature, if any. The speculation could be validated limited at room temperature, because the interlayer exchange interaction was remarkably different between two samples at low temperatures [51].

C. Spin Hall angles evaluated via ST-FMR

Because the effective demagnetization field (M_{eff}) is required to estimate the θ_{SH} as shown in Eq. (8), we first analyzed the FMR spectra observed in the measurement of ST-FMR [Fig. 3(a)]. The blue magnetic wire shown in Fig. 3(a) connects to the coplanar waveguide made of patterned Cu films. The rectified dc voltage (V_{mix}), originating from the magnetization precession in the CFB layer induced by the ac current from the signal generator, was recorded using

the lock-in amplifier and the broadband bias tee circuit. The direction of ac current (x axis) corresponds to the [100] direction of the unit cell of MPN and MP. The in-plane magnetic field (H) was applied at an azimuthal angle (φ) with respect to the y axis.

The inset of Fig. 3(a) shows the representative V_{mix} as a function of H with $\varphi = 45^\circ$ and $f = 8$ GHz for the MPN/CFB sample. The V_{mix} can be reproduced by the combination of symmetrical Lorentzian (V_s) and antisymmetrical Lorentzian (V_a) components as [54]

$$V_{\text{mix}} = V_s \frac{\Delta H^2}{\Delta H^2 + (H - H_r)^2} + V_a \frac{\Delta H(H - H_r)}{\Delta H^2 + (H - H_r)^2}, \quad (3)$$

where ΔH and H_r are the FMR linewidth and the resonance field, respectively. The experimental data plots can be fitted well with Eq. (3) by using the fitting parameters, $V_s = 0.59 \mu\text{V}$, $V_a = 1.4 \mu\text{V}$, $\mu_0 \Delta H = 4.8$ mT, and $\mu_0 H_r = 55$ mT, as shown by the solid lines.

Figure 3(b) shows the correlation between f and H_r to estimate the M_{eff} for the CFB layer on both the MPN and MP layers. The plots were fitted by Kittel's formula for in-plane magnetized ferromagnetic films [55],

$$f = \frac{\gamma}{2\pi} \mu_0 \sqrt{H(H + M_{\text{eff}})}, \quad (4)$$

where γ represents the gyromagnetic ratio. The dashed lines reproduced the plots using Eq. (4) with the $\mu_0 M_{\text{eff}} = 1.12$ T for the MPN/CFB and 1.03 T for the MP/CFB. Here, we define the effective demagnetization field as the superposition of the anisotropy field: $\mu_0 M_{\text{eff}} = \mu_0 M_s - \frac{2K_u}{\mu_0 M_s}$, where K_u represents the uniaxial magnetic anisotropy energy density, originating predominantly from the MPN/CFB and MP/CFB interfaces. Therefore, the second term $\frac{2K_u}{\mu_0 M_s}$ corresponds to the anisotropy field applied in the perpendicular direction of film plane, which was estimated to be 0.41 T for the MPN/CFB and 0.409 T for the MP/CFB. Note that these similar anisotropy fields are strongly supported by the fact that the interlayer exchange interaction for both samples is similar at room temperature, as explained in Fig. 2(c). Figure 3(c) shows the correlation between ΔH and f , which allows for assessing the effective damping factor (α_{eff}) of the CFB layer on the MPN and MP layers. The plots were fitted by Kittel's formula [55],

$$\mu_0 \Delta H = \frac{2\pi f \alpha_{\text{eff}}}{\gamma} + \mu_0 \Delta H_0. \quad (5)$$

The dashed lines reproduced the plots employing Eq. (5) with $\alpha_{\text{eff}} \approx 0.0122$ for the MPN/CFB and 0.0138 for the MP/CFB, indicating similar values for both samples. We thus infer that the intrinsic and/or extrinsic line-broadening mechanisms at the interface of MPN/CFB are comparable to those of MP/CFB.

In order to investigate the characteristics of SOTs, we evaluated the dependence of V_s and V_a on φ for both MPN/CFB and MP/CFB. The V_s and V_a are generally caused by the current-induced damping-like (DL) torque ($m \times \sigma_y \times m$) and field-like torque (FL) ($m \times \sigma_y$) acting, respectively, on the magnetization (m) of adjacent ferromagnetic layers. This occurs in the conventional heavy-metal-ferromagnet systems, where the dominant spin current is induced by σ_y via the ordinary SHE. However, the SOTs also arise from additional spin components such as σ_x and σ_z in the case of noncollinear AFMs. Therefore, the equations for the extended signals in ST-FMR are given by [3,5,24,38,39],

$$V_s = V_{x,\text{DL}} \sin 2\varphi \sin \varphi + V_{y,\text{DL}} \sin 2\varphi \cos \varphi + V_{z,\text{FL}} \sin 2\varphi, \quad (6)$$

$$V_a = V_{x,\text{FL}} \sin 2\varphi \sin \varphi + (V_{y,\text{FL}+\text{Oe}}) \sin 2\varphi \cos \varphi + V_{z,\text{DL}} \sin 2\varphi, \quad (7)$$

where $V_{s,\text{DL(FL)}}$ ($s = x, y, \text{ and } z$) represents the measured voltage generated by the DL (FL) torque due to σ_s . Figures 3(d) and 3(e) show the dependence of V_s and V_a on φ for the MPN/CFB and the MP/CFB, respectively. We used Eqs. (6) and (7) to fit the plots, and found that the dominant SOT is associated with σ_y as the conventional SHE in heavy metals. However, further analysis suggested the coexistence of σ_x and σ_z components, although the contribution was minor (Table I).

The estimation of θ_{SH} relies on the ratio of the V_s and V_a components found in the ST-FMR spectra as [56]

$$\theta_{\text{SH}} = \frac{V_s}{V_a} \frac{e\mu_0 M_s d_{\text{AFM}} d_{\text{CFB}}}{\hbar} \sqrt{1 + \frac{\mu_0 M_{\text{eff}}}{\mu_0 H_r}}, \quad (8)$$

TABLE I. Fitting parameters of Eqs. (6) and (7) to reproduce the plots in Figs. 3(d) and 3(e), where the unit is μV .

	$V_{x,\text{DL(FL)}}$	$V_{y,\text{DL(FL}+\text{Oe)}}$	$V_{z,\text{DL(FL)}}$
MPN/CFB	~ 0 (-0.20)	1.7 (3.6)	~ 0 (~ 0)
MP/CFB	~ 0 (-0.20)	1.3 (2.8)	0.10 (~ 0)

where e , μ_0 , $d_{\text{AFM(CFB)}}$, and \hbar represent the elementary charge, the vacuum permeability, the film thickness of MP and MPN (CFB) layer, and Dirac's constant, respectively. Assuming that σ_y dominates the entire SOT, the θ_{SH} of MPN (MP) was estimated to be 0.033 ± 0.0045 (0.025 ± 0.0035) for $f = 8$ GHz using Eq. (8), with $\mu_0 M_s \approx 1.58$ T (1.40 T), $\mu_0 M_{\text{eff}} \approx 0.11$ T (0.10 T), and $V_s/V_a \approx V_{y,\text{DL}}/V_{y,\text{FL}+\text{Oe}} = 0.53 \pm 0.065$ (0.46 ± 0.064). It was evident that the charge to y-spin conversion efficiency in the MPN was greater than that in the MP. These are also confirmed regardless of f from 7 GHz to 10 GHz [Fig. 3(f)], and the θ_{SH} increased with increasing d_{AFM} [Fig. 3(g)]. Taking into account the tetragonal distortion depending on thickness d_{MPN} [51], the Γ_{4g} -type noncollinear AFM structure could be stable and predominant by increasing d_{AFM} . These results provide insight into the relationship between the θ_{SH} and the stability of magnetic structures.

D. SOT effective fields evaluated via second-harmonic Hall measurements

To confirm the fact that θ_{SH} for σ_y of the MPN was greater than that of the MP, the second-harmonic Hall measurement was performed at room temperature with the measurement configuration shown in Fig. 4(a). Figure 4(b) shows the evaluation of the resistivity of MPN, MP, and CFB layers based on the dc four-point-probe resistance measurements for the samples with various CFB thicknesses. The ρ_{MPN} , ρ_{MP} , and ρ_{CFB} were measured to be 109, 125, and 140 $\mu\Omega$ cm, respectively. Here we used the formula $R_{xx}^{-1}(\frac{L}{W}) = \frac{d_{\text{CFB}}}{\rho_{xx}^{\text{CFB}}} + \frac{d_{\text{AFM}}}{\rho_{xx}^{\text{AFM}}}$ for analysis, where d_{CFB} is the thickness of CFB layer and d_{AFM} is the thicknesses of MP and MPN layers. We confirmed that the ρ_{CFB} was comparable to the previous study [57]. Figures 4(c) and 4(d) show the representative second-harmonic Hall voltages ($V_{xy}^{2\omega}$) as a function of the azimuthal angle (φ) of in-plane external field (H_{inp}) with respect to the direction of ac current flow (I_{ac}) for the MPN/CFB and MP/CFB samples, respectively, where we applied $I_{\text{ac}} = 2$ mA ($J_{\text{ac}} \approx 2.5 \times 10^6$ A/cm²) and $\mu_0 H_{\text{inp}} = 50$ mT. Since the component of σ_y dominates the SOT origin, judging from the ST-FMR results, the $V_{xy}^{2\omega}$ was decomposed by using the following equations [58,59]:

$$V_{xy}^{2\omega} = V_{\text{DL}} + V_{\text{FL}+\text{Oe}} + V_{\text{ANE}} = -A \cos \varphi + B(2\cos^3 \varphi - \cos \varphi), \quad (9)$$

$$A = V_{\text{AHE}} \frac{H_{\text{DL}}}{H + H_{\text{k}}} + V_{\text{ANE}}, \quad (10)$$

$$B = 2V_{\text{PHE}} \frac{H_{\text{FL}+\text{Oe}}}{H}. \quad (11)$$

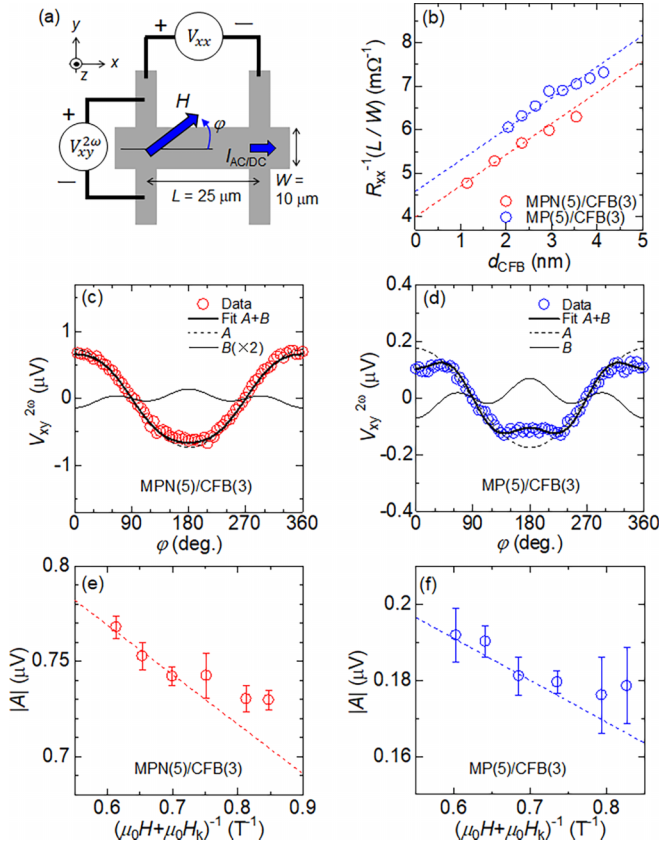


FIG. 4. (a) Measurement configuration of the second-harmonic Hall voltage. (b) Electric conductance as a function of the CoFeB layer thickness (d_{CFB}). The dashed lines represent the fitting results using the formula $R_{xx}^{-1}(L/W) = \frac{d_{\text{CFB}}}{\rho_{xx}^{\text{CFB}}} + \frac{d_{\text{AFM}}}{\rho_{xx}^{\text{AFM}}}$. (c), (d) Second-harmonic Hall voltage ($V_{xy}^{2\omega}$) as a function of azimuthal angle of in-plane field (ϕ) with $I_{\text{ac}} = 2$ mA and $H_{\text{ext}} = 50$ mT. Solid and dashed lines represent the fitting results by Eqs. (9)–(11). (e), (f) Fitting parameter $|A|$ under the various H , where H_k represents the anisotropy field evaluated by AHE (see Fig. S4 in Supplemental Material [51]). Dashed lines represent the linear fit to the plots for higher H region to obtain the H_{DL} as shown by Eq. (10).

$V_{\text{PHE(AHE)}}$, V_{DL} , $V_{\text{FL+Oe}}$, and V_{ANE} represent the measured voltage originating from the planar Hall effect (anomalous Hall effect as shown in Ref. [51]), the DL torque, the total of FL torque and current-induced field, and anomalous Nernst effect, respectively. The anisotropy field (H_k) was defined as the saturation magnetic field in the hysteresis loop of AHE as shown in Ref. [51]. The data in Figs. 4(c) and 4(d) can be fitted by Eqs. (9)–(11) with the best parameters A and B . Although A is contaminated by the component of ANE, note that the component of H_{DL} can be separated as the slope of linear fit to the plots of A vs $(H + H_k)^{-1}$ as shown in Eq. (10). Therefore, the measurements of $V_{xy}^{2\omega}$ with various H were performed as shown in Figs. 4(e) and 4(f). The A for weak H showed a different trend compared to that for strong H , so we excluded these data from the linear fit. Consequently, the $|H_{\text{DL}}|$ values were estimated to be $\sim 0.383 \pm 0.0056$ mT/(MA cm $^{-2}$) for the MPN/CFB and $\sim 0.291 \pm 0.011$ mT/(MA cm $^{-2}$) for the MP/CFB. The

results demonstrate the positive effect of N for SOT, which qualitatively agreed with the conclusion by ST-FMR.

E. Spin Hall conductivity based on first-principles calculation

In discussion, the spin conductivities with each polarization when the charge and spin current, respectively, flow along x - and z direction [see coordinates described in Figs. 1(a) and 3(a)], $\sigma_{xz}^y(E)$, $\sigma_{xz}^x(E)$, and $\sigma_{xz}^z(E)$, were calculated for the MP and MPN as shown in Figs. 5(a)–5(c). Note that the lattice constants of MP and MPN were set to be $a = b = 0.40046$ nm and $c = 0.395$ nm, which are the realistic values of the 5-nm-thick MPN film evaluated via XRD structural analysis (Fig. 1(b) and Ref. [51]), in order to discuss the pure contribution of N. We confirmed that the Γ_{4g} -type noncollinear AFM structures for three face-centered Mn atoms with head-to-head and tail-to-tail configuration on the (111) plane are energetically more stable than the collinear ferromagnetic structures on the (100) plane. Although finite spin conductivities were found for all components, the $\sigma_{xz}^y(E_F)$ for MPN increased at the E_F compared to MP. Note that the enhancement is significant for $\sigma_{xz}^y(E_F)$ rather than those of $\sigma_{xz}^x(E_F)$ and $\sigma_{xz}^z(E_F)$. These results are consistent with the present experimental results shown in Table I. We show the spin Berry curvature $\Omega_{xz}^y(\mathbf{k}, E_F)$ along the high-symmetry line of MP and MPN in Fig. 5(d). It was revealed that the $\Omega_{xz}^y(\mathbf{k}, E_F)$ along the A-Z-R line of MPN was much larger than that of MP, which could be a possible mechanism of the enhanced $\sigma_{xz}^y(E_F)$ in the MPN. It is inferred that the large $\Omega_{xz}^y(\mathbf{k}, E_F)$ along the A-Z-R line of MPN can be attributed to the hybridization of Mn- d and N- p orbitals [51]. In order to provide an insight into the hybridization effect, we investigated the projection of each atomic orbital on the band dispersion along the high-symmetry line as shown in Figs. 5(e) and 5(f). The bands around the E_F of MP are mainly composed of d orbitals of Mn and Pt, while those of MPN are mainly composed of Mn and N orbital components especially along the A-Z-R line. In addition, the dominant component of N orbital presents ~ -1.0 eV as well. Therefore, these bands are mainly responsible for the large $\Omega_{xz}^y(\mathbf{k}, E_F)$ in MPN system as shown in Fig. 5(d), leading to the enhancement of $\sigma_{xz}^y(E_F)$ due to the $p-d$ dipole transition in MPN as compared to MP [60].

Understanding the impact of ordering or vacancy at the N site in the antiperovskites is crucial due to its direct correlation with the band dispersion near the E_F as predicted by the calculation mentioned above. In antiperovskites such as Mn_3BN , in which N and Mn atoms form a stable octahedral structure, the narrow band near the E_F is primarily composed of d orbitals of Mn and p orbitals of N [40]. Therefore, the magnetic and transport properties are influenced strongly by the presence of N, and the enhanced charge-to-spin conversion obtained in this study might be one of the positive properties caused by N. Although the present study emphasizes the significance of N in the Mn-based AFM antiperovskite Mn_3BN with $B = \text{Pt}$, this might be applicable to various B , judging from the previous reports on the Mn_3GaN [38] and Mn_3MnN (denoted by Mn_4N) films [24,61] with highly efficient current-induced magnetization switching by SOT. Therefore, selecting the other candidates of B that can maximize the effect of N might be a remaining issue from the perspective of material

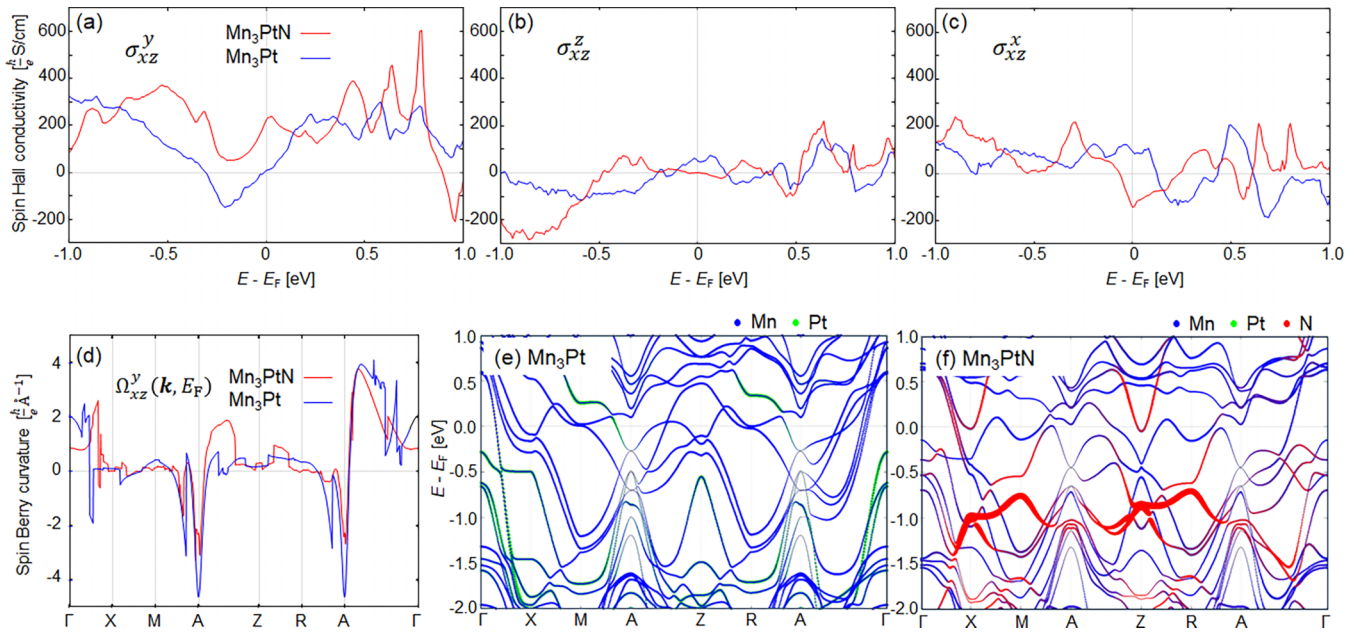


FIG. 5. (a)–(c) Calculated spin Hall conductivities for MP and MPN $\sigma_{\alpha\beta}^{\gamma}$ as a function of energy (E) relative to the Fermi level (E_F), where α , β , and γ are the direction of current flow, the direction of spin current, and the polarization direction of the spin (spin quantum axis), respectively. (d) Spin Berry curvature at the E_F along the high-symmetry line in the first Brillouin zone for Mn_3Pt and Mn_3PtN . (e), (f) Projections of each atomic orbital on the band dispersions of Mn_3Pt and Mn_3PtN along high-symmetry line around the E_F . The projections on N orbitals are magnified by a factor of 3 compared to other atomic orbitals. The high-symmetry k points (x, y, z) are $\Gamma(0, 0, 0)$, $X(0, 1/2, 0)$, $M(1/2, 1/2, 0)$, $A(1/2, 1/2, 1/2)$, $Z(0, 0, 1/2)$, and $R(0, 1/2, 1/2)$ in the Brillouin zone $xb_1 + yb_2 + zb_3$, respectively. The b_1 , b_2 , b_3 are the reciprocal vectors of the tetragonal cell.

engineering for efficient charge-to-spin conversion without the need for heavy metals.

IV. CONCLUSION

The impact of N on the charge-to-spin conversion was investigated by comparing the MPN/CFB and MP/CFB bilayers. Both MPN and MP films deposited on the MgO substrate involved tetragonal distortion with a lattice constant ratio of $c/a \approx 0.99$. The presence of AHE indicates a possible magnetic structure of the Γ_{4g} -type. The angular-dependent ST-FMR revealed the dominant contribution of σ_y as in the conventional SHE of heavy metals. Furthermore, the θ_{SH} based on the σ_y of MPN was greater than that of MP. These findings were supported by the second harmonic Hall measurements and first-principles calculation of σ_{xz}^y at the E_F . N

plays a crucial role to stabilize the Γ_{4g} -type magnetic structure and provide the advantages to boost intrinsic σ_{xz}^y dominantly due to the Mn(d)-N(p) hybridized band in the A-Z-R line toward the E_F .

ACKNOWLEDGMENTS

The authors thank Mr. T. Morita at NIMS for technical support. This work was supported by KAKENHI Grants-in-Aid No. 23K22803 from the Japan Society for the Promotion of Science (JSPS). Part of this work was carried out under the Cooperative Research Project Program of the RIEC, Tohoku University. N.T. received support from the DST-INSPIRE Fellowship and NIMS-ICGP internship program. IIT (BHU), Varanasi, is acknowledged for partial support. The AXRD measurements were performed at the BL13XU of SPring-8.

- [1] Y. K. Kato, R. C. Myers, A. C. Gossard, and D. D. Awschalom, Observation of the spin Hall effect in semiconductors, *Science* **306**, 1910 (2004).
- [2] H. J. Zhang, S. Yamamoto, B. Gu, H. Li, M. Maekawa, Y. Fukaya, and A. Kawasuso, Charge-to-spin conversion and spin diffusion in Bi/Ag bilayers observed by spin-polarized positron beam, *Phys. Rev. Lett.* **114**, 166602 (2015).
- [3] L. Yu, S. Karube, M. Liu, M. Tsunoda, M. Oogane, and Y. Ando, Observation of unconventional spin-polarization induced spin-orbit torque in $L1_2$ -ordered antiferromagnetic Mn_3Pt thin films, *Appl. Phys. Express* **15**, 033002 (2022).
- [4] H. Bai, X. F. Zhou, H. W. Zhang, W. W. Kong, L. Y. Liao, X. Y. Feng, X. Z. Chen, Y. F. You, Y. J. Zhou, L. Han, W. X. Zhu, F. Pan, X. L. Fan, and C. Song, Control of spin-orbit torques through magnetic symmetry in differently oriented noncollinear antiferromagnetic Mn_3Pt , *Phys. Rev. B* **104**, 104401 (2021).
- [5] C. Cao, S. Chen, R. C. Xiao, Z. Zhu, G. Yu, Y. Wang, X. Qiu, L. Liu, T. Zhao, D. F. Shao, Y. Xu, J. Chen, and Q. Zhan, Anomalous spin current anisotropy in a noncollinear antiferromagnet, *Nat. Commun.* **14**, 5873 (2023).
- [6] T. Nan, C. X. Quintela, J. Irwin, G. Gurung, D. F. Shao, J. Gibbons, N. Campbell, K. Song, S.-Y. Choi, L. Guo, R. D.

- Johnson, P. Manuel, R. V. Chopdekar, I. Hallsteinsen, T. Tybell, P. J. Ryan, J.-W. Kim, Y. Choi, P. G. Radaelli, D. C. Ralph, E. Y. Tsymbal, M. S. Rzechowski, and C. B. Eom, Controlling spin current polarization through non-collinear antiferromagnetism, *Nat. Commun.* **11**, 4671 (2020).
- [7] S. Husain, N. F. Prestes, O. Fayet, S. Collin, F. Godel, E. Jacquet, T. Denneulin, R. E. Dunin-Borkowski, A. Thiaville, M. Bibes, H. Jaffres, N. Reyren, A. Fert, and J.-M. George, Field-free switching of perpendicular magnetization in an ultrathin epitaxial magnetic insulator, *Nano Lett.* **24**, 2743 (2024).
- [8] E. Krén, G. Kádár, L. Pál, J. Sólyom, P. Szabó, and T. Tarnóczy, Magnetic structures and exchange interactions in the Mn-Pt system, *Phys. Rev.* **171**, 574 (1968).
- [9] H. Chen, Q. Niu, and A. H. MacDonald, Anomalous Hall effect arising from noncollinear antiferromagnetism, *Phys. Rev. Lett.* **112**, 017205 (2014).
- [10] S. Isogami and Y. K. Takahashi, Antiperovskite magnetic materials with 2p light elements for future practical applications, *Adv. Electron. Mater.* **9**, 2200515 (2023).
- [11] K. Ito, S. Honda, and T. Suemasu, Transition metal nitrides and their mixed crystals for spintronics, *Nanotechnology* **33**, 062001 (2022).
- [12] Z. Zhang and W. Mi, Synthesis and characterization of the high-hardness magnetic material $\text{Mn}_2\text{N}_{0.86}$, *J. Phys. D: Appl. Phys.* **55**, 013001 (2022).
- [13] J. M. D. Coey, D. Givord, and D. Fruchart, Metallic nitride and carbide perovskites: History and prospects, *ECS J. Solid State Sci. Technol.* **11**, 055002 (2022).
- [14] J. Cui, M. Kramer, L. Zhou, F. Liu, A. Gabay, G. Hadjipanayis, B. Balasubramanian, and D. Sellmyer, Current progress and future challenges in rare-earth-free permanent magnets, *Acta Mater.* **158**, 118 (2018).
- [15] H. K. Singh, I. Samathrakris, N. M. Fortunato, J. Zemen, C. Shen, O. Gutfleisch, and H. Zhang, Multifunctional antiperovskites driven by strong magneto-structural coupling, *npj Comput. Mater.* **7**, 98 (2021).
- [16] K. Sunaga, M. Tsunoda, K. Komagaki, Y. Uehara, and M. Takahashi, Inverse tunnel magnetoresistance in magnetic tunnel junctions with a Fe_4N electrode, *J. Appl. Phys.* **102**, 013917 (2007).
- [17] Y. Komasaki, M. Tsunoda, S. Isogami, and M. Takahashi, Negative anisotropic magnetoresistance in Fe_4N film, *J. Appl. Phys.* **105**, 07C928 (2009).
- [18] Y. Komasaki, M. Tsunoda, S. Isogami, C. C. Chen, and M. Takahashi, Dependence of magnetic damping on temperature and crystal orientation in epitaxial Fe_4N thin films, *J. Magn. Soc. Jpn.* **34**, 524 (2010) (in Japanese).
- [19] M. Tsunoda, Y. Komasaki, S. Kokado, S. Isogami, C. C. Chen, and M. Takahashi, Negative anisotropic magnetoresistance in Fe_4N film, *Appl. Phys. Express* **2**, 083001 (2009).
- [20] X. Li, H. Li, M. Jamali, and J. P. Wang, Damping constant measurement and inverse giant magnetoresistance in spintronic devices with Fe_4N , *AIP Adv.* **7**, 125303 (2017).
- [21] S. Isogami, M. Tsunoda, Y. Komasaki, A. Sakuma, and M. Takahashi, Inverse current-induced magnetization switching in magnetic tunnel junctions with Fe_4N free layer, *Appl. Phys. Express* **3**, 103002 (2010).
- [22] H. Li, G. Wang, D. Li, P. Hu, W. Zhou, X. Ma, S. Dang, S. Kang, T. Dai, F. Yu, X. Zhou, S. Wu, and S. Li, Spin-orbit torque-induced magnetization switching in epitaxial $\text{Au}/\text{Fe}_4\text{N}$ bilayer films, *Appl. Phys. Lett.* **114**, 092402 (2019).
- [23] H. Li, G. Wang, D. Li, P. Hu, W. Zhou, S. Dang, X. Ma, T. Dai, S. Kang, F. Yu, X. Zhou, S. Wu, and S. Li, Field-free deterministic magnetization switching with ultralow current density in epitaxial $\text{Au}/\text{Fe}_4\text{N}$ bilayer films, *ACS Appl. Mater. Interfaces* **11**, 16965 (2019).
- [24] H. Bai, T. Xu, Y. Dong, H.-A. Zhou, and W. Jiang, Spin-torque switching in rare-earth-free compensated ferrimagnet Mn_4N films, *Adv. Electron. Mater.* **8**, 2100772 (2021).
- [25] H. Sakakibara, H. Ando, Y. Kuroki, S. Kawai, K. Ueda, and H. Asano, Magnetic properties and anisotropic magnetoresistance of antiperovskite nitride $\text{Mn}_3\text{GaN}/\text{Co}_3\text{FeN}$ exchange-coupled bilayers, *J. Appl. Phys.* **117**, 17D725 (2015).
- [26] S. Isogami, K. Takanashi, and M. Mizuguchi, Dependence of anomalous Nernst effect on crystal orientation in highly ordered γ' - Fe_4N films with anti-perovskite structure, *Appl. Phys. Express* **10**, 073005 (2017).
- [27] S. Isogami, K. Masuda, Y. Miura, N. Rajamanickam, and Y. Sakuraba, Anomalous Hall and Nernst effects in ferrimagnetic Mn_4N films: Possible interpretations and prospects for enhancement, *Appl. Phys. Lett.* **118**, 092407 (2021).
- [28] K. Ito, J. Wang, Y. Shimada, H. Sharma, M. Mizuguchi, and K. Takanashi, Enhancement of the anomalous Nernst effect in epitaxial Fe_4N films grown on $\text{SrTiO}_3(001)$ substrates with oxygen-deficient layers, *J. Appl. Phys.* **132**, 133904 (2022).
- [29] B. W. Qiang, N. Togashi, S. Momose, T. Wada, T. Hajiri, M. Kuwahara, and H. Asano, Room-temperature magnetic skyrmion in epitaxial thin films of $\text{Fe}_{2-x}\text{Pd}_x\text{Mo}_3\text{N}$ with the filled β -Mn-type chiral structure, *Appl. Phys. Lett.* **117**, 142401 (2020).
- [30] S. Ghosh, T. Komori, A. Hallal, J. P. Garcia, T. Gushi, T. Hirose, H. Mitarai, H. Okuno, J. Vogel, M. Chshiev, J.-P. Attané, L. Vila, T. Suemasu, and S. Pizzini, Current-driven domain wall dynamics in ferrimagnetic Ni-doped Mn_4N films: Very large domain wall velocities and reversal of motion direction across the magnetic compensation point, *Nano Lett.* **21**, 2580 (2021).
- [31] C. T. Ma, T. Q. Hartnett, W. Zhou, P. V. Balachandran, and S. J. Poon, Tunable magnetic skyrmions in ferrimagnetic Mn_4N , *J. Appl. Phys.* **119**, 192406 (2021).
- [32] H. Vakili, J. W. Xu, W. Zhou, M. N. Sakib, M. G. Morshed, T. Hartnett, Y. Quessab, K. Litzius, C. T. Ma, S. Ganguly, M. R. Stan, P. V. Balachandran, G. S. D. Beach, S. J. Poon, A. D. Kent, and A. W. Ghosh, Skyrmionics-Computing and memory technologies based on topological excitations in magnets, *J. Appl. Phys.* **130**, 070908 (2021).
- [33] T. Gushi, M. J. Klug, J. P. Garcia, S. Ghosh, J.-P. Attané, H. Okuno, O. Fruchart, J. Vogel, T. Suemasu, S. Pizzini, and L. Vila, Large current driven domain wall mobility and gate tuning of coercivity in ferrimagnetic Mn_4N thin films, *Nano Lett.* **19**, 8716 (2019).
- [34] Y. Maeda, K. Imamura, M. Ohtake, S. Isogami, T. Kawai, M. Futamoto, F. Kirino, and N. Inaba, Large magnetostriction in γ' - Fe_4N single-crystal thin film, *J. Magn. Magn. Mater.* **585**, 170942 (2023).
- [35] T. Bayarara, V. Ivanov, L. Z. Tan, and S. M. Griffin, Intrinsic origin and enhancement of topological responses in ferrimagnetic antiperovskite Mn_4N , *Phys. Rev. B* **109**, 014430 (2024).

- [36] X. Zhou, J. P. Hanke, W. Feng, S. Blügel, Y. Mokrousov, and Y. Yao, Giant anomalous Nernst effect in noncollinear antiferromagnetic Mn-based antiperovskite nitrides, *Phys. Rev. Mater.* **4**, 024408 (2020).
- [37] V. T. N. Huyen, M. Suzuki, K. Yamauchi, and T. Oguchi, Topology analysis for anomalous Hall effect in the noncollinear antiferromagnetic states of Mn_3AN ($A = Ni, Cu, Zn, Ga, Ge, Pd, In, Sn, Ir, Pt$), *Phys. Rev. B* **100**, 094426 (2019).
- [38] T. Hajiri, S. Ishino, K. Matsuura, and H. Asano, Electrical current switching of the noncollinear antiferromagnet Mn_3GaN , *Appl. Phys. Lett.* **115**, 052403 (2019).
- [39] Y. You, H. Bai, X. Feng, X. Fan, L. Han, X. Zhou, Y. Zhou, R. Zhang, T. Chen, F. Pan, and C. Song, Cluster magnetic octupole induced out-of-plane spin polarization in antiperovskite antiferromagnet, *Nat. Commun.* **12**, 6524 (2021).
- [40] R. Chou, Y. Sun, H. Lu, and G.-H. Lu, Structure, magnetic properties and thermal expansion of Mn_3PtN ($0 \leq x \leq 1.0$) compounds, *Int. J. Mod. Phys. B* **32**, 1850314 (2018).
- [41] A. Anzai, T. Gushi, T. Komori, S. Honda, S. Isogami, and T. Suemasu, Transition from minority to majority spin transport in iron-manganese nitride $Fe_{4-x}Mn_xN$ films with increasing x , *J. Appl. Phys.* **124**, 123905 (2018).
- [42] S. Isogami, A. Anzai, T. Gushi, T. Komori, and T. Suemasu, Temperature independent, wide modulation of anomalous Hall effect by Mn doping in $Fe_{4-x}Mn_xN$ pseudo-single-crystal films, *Jpn. J. Appl. Phys.* **57**, 120305 (2018).
- [43] P. Giannozzi, S. Baroni, N. Bonini, M. Calandra, R. Car, C. Cavazzoni, D. Ceresoli, G. L. Chiarotti, M. Cococcioni, I. Dabo, A. D. Corso, S. de Gironcoli, S. Fabris, G. Fratesi, R. Gebauer, U. Gerstmann, C. Gougousis, A. Kokalj, M. Lazzeri, L. Martin-Samos *et al.*, QUANTUM ESPRESSO: A modular and open-source software project for quantum simulations of materials, *J. Phys.: Condens. Matter* **21**, 395502 (2009).
- [44] P. E. Blöchl, Projector augmented-wave method, *Phys. Rev. B* **50**, 17953 (1994).
- [45] J. P. Perdew, K. Burke, and M. Ernzerhof, Generalized gradient approximation made simple, *Phys. Rev. Lett.* **77**, 3865 (1996).
- [46] H. Nakano, A method of calculation of electrical conductivity, *Prog. Theor. Phys.* **15**, 77 (1956).
- [47] R. Kubo, Statistical mechanical theory of irreversible processes: General theory and simple applications in magnetic and conduction problems, *J. Phys. Soc. Jpn.* **12**, 570 (1957).
- [48] Y. Miura and K. Masuda, First-principles calculations on the spin anomalous Hall effect of ferromagnetic alloys, *Phys. Rev. Mater.* **5**, L101402 (2021).
- [49] N. Marzari and D. Vanderbilt, Maximally localized generalized Wannier functions for composite energy bands, *Phys. Rev. B* **56**, 12847 (1997).
- [50] I. Souza, N. Marzari, and D. Vanderbilt, Maximally localized Wannier functions for entangled energy bands, *Phys. Rev. B* **65**, 035109 (2001).
- [51] See Supplemental Material at <http://link.aps.org/supplemental/10.1103/PhysRevB.109.224406> for Sec. I the atomic ordering of Mn evaluated using anomalous XRD (AXRD) with the synchrotron radiation soft x ray; Sec. S2 the thickness dependence of lattice constant and tetragonal distortion; see Sec. S3 for the temperature dependence of inter-layer exchange interaction; see Sec. S4 for the anomalous Hall measurements for SOT evaluation; see Sec. S5 for the impact of N to the density of states and band dispersion; and which includes Refs. [62,63].
- [52] G. Gurung, D. F. Shao, T. R. Paudel, and E. Y. Tsymbal, Anomalous Hall conductivity of noncollinear magnetic antiperovskites, *Phys. Rev. Mater.* **3**, 044409 (2019).
- [53] I. Samathrakris and H. B. Zhang, Tailoring the anomalous Hall effect in the noncollinear antiperovskite Mn_3GaN , *Phys. Rev. B* **101**, 214423 (2020).
- [54] N. Mecking, Y. S. Gui, and C.-M. Hu, Microwave photovoltage and photo-resistance effects in ferromagnetic microstrips, *Phys. Rev. B* **76**, 224430 (2007).
- [55] C. Kittel, On the theory of ferromagnetic resonance absorption, *Phys. Rev.* **73**, 155 (1948).
- [56] L. Liu, T. Moriyama, D. C. Ralph, and R. A. Buhrman, Spin-torque ferromagnetic resonance induced by the spin Hall effect, *Phys. Rev. Lett.* **106**, 036601 (2011).
- [57] Y. C. Lau and M. Hayashi, Spin torque efficiency of Ta, W, and Pt in metallic bilayers evaluated by harmonic Hall and spin Hall magnetoresistance measurements, *Jpn. J. Appl. Phys.* **56**, 0802B5 (2017).
- [58] S. Isogami, Spin-orbit torques in antiperovskite Fe_4N pseudo-single-crystal films with negative spin polarization, *J. Magn. Magn. Mater.* **501**, 166400 (2020).
- [59] M. Hayashi, J. Kim, M. Yamanouchi, and H. Ohno, Quantitative characterization of the spin-orbit torque using harmonic Hall voltage measurements, *Phys. Rev. B* **89**, 144425 (2014).
- [60] P. Bruno, Y. Suzuki, and C. Chappert, Magneto-optical Kerr effect in a paramagnetic overlayer on a ferromagnetic substrate: A spin-polarized quantum size effect, *Phys. Rev. B* **53**, 9214 (1996).
- [61] S. Isogami, N. Rajamanickam, Y. Kozuka, and Y. K. Takahashi, Efficient current-driven magnetization switching owing to isotropic magnetism in a highly symmetric 111-oriented N epitaxial single layer, *AIP Adv.* **11**, 105314 (2021).
- [62] T. Nakatani, S. K. Narayananellore, L. S. R. Kumara, H. Tajiri, Y. Sakuraba, and K. Hono, Thickness dependence of degree of $B2$ order of polycrystalline $Co_2(Mn_{0.6}Fe_{0.4})$ Ge Heusler alloy films measured by anomalous X-ray diffraction and its impacts on current-perpendicular-to-plane giant magnetoresistance properties, *Scr. Mater.* **189**, 63 (2020).
- [63] H. Tajiri, L. S. R. Kumara, Y. Sakuraba, Z. Chen, J. Wang, W. Zhou, K. Varun, K. Ueda, S. Yamada, K. Hamaya, and K. Hono, Structural insight using anomalous XRD into Mn_2CoAl Heusler alloy films grown by magnetron sputtering, IBAS, and MBE techniques, *Acta Mater.* **235**, 118063 (2022).